nature communications

Article

https://doi.org/10.1038/s41467-025-63827-y

Electro-manipulating of negative-charged aramid nanofibers towards micro-to-macro scale colloidal aerogel films

Received: 24 April 2025

Accepted: 22 August 2025

Published online: 30 September 2025

Check for updates

Lishan Li[1], Ruomei Yin[1], Zhizhi Sheng[1] & Xuetong Zhang[1,2]

Aerogels, often hailed as the world-changing magic nanoporous material, are traditionally synthesized through reagent-induced sol-gel transitions. However, the uncontrolled random motion of molecular/colloidal precursors poses significant challenges in achieving precise structural control of aerogel. In this study, we present an unprecedented electro-manipulation strategy, easy to be applied in batch-run as well as roll-to-roll processes, to engineer well-defined micro-/macro-structured aerogel films. By leveraging electrophoresis-driven self-assembly and electrochemistry-driven gelation of negatively charged aramid nanofibers in sequence, we demonstrate large-area (50 cm × 50 cm) as well as continuous (up to 20 meters in length) fabrications of aramid colloidal aerogel films with patterned microstructures and programmable nanofiber orientation. These features effectively enhance the performance of the resulting colloidal aerogel films such as mechanical strength, thermal insulation and proton conduction, and show their broad applications in various fields. This work presents an effective strategy for precise aerogel structure regulation through external field manipulation.

Aerogels, a class of ultralight nanoporous materials synthesized via sol-gel processes, were recognized by Science as one of the ten emerging materials poised to transform global technologies[1–5]. These materials are broadly categorized into molecular aerogels, derived from small-molecule precursors via hydrolysis-condensation reactions[6–8], and colloidal aerogels formed through sol-gel transitions of nanomaterial dispersions[9–12]. The latter category offers particular advantages, enabling both efficient utilization of low-dimensional nanomaterials and bottom-up construction of complex porous architectures with precisely tailorable functionality. Conventional fabrication methods for both types predominantly rely on chemical induction strategies, where additives (e.g., acids, alkalis, or crosslinkers) initiate sol destabilization or chemical crosslinking. However, uncontrolled molecular/colloidal migration and stochastic self-assembly during chemically driven sol-gel transitions pose significant challenges to achieving controllable aerogels with hierarchical structure.

The inherent surface charges of colloidal nanoparticles make them highly responsive to external electrical fields, offering a promising platform for electro-manipulating migration, assembly, and gelation to fabricate aerogels with precisely defined structures. Among various electro-manipulation techniques, electrophoresis stands out as a well-established method, enabling precise colloidal control through directional migration, spatial confinement, and ordered assembly. For instance, Hayward's team[13] utilized electrophoretic assembly to create colloidal crystal arrays with tunable optical properties, while Li et al[14]. enhanced quantum efficiency in luminescent films by electrophoretic depositing SiO_2/TiO_2 colloids embedded with quantum dots. However, electrophoretic deposition (EPD) often induces dense packing film but not gel, necessitating synergistic integration with electrochemical gelation, a technique constructing chemically crosslinked networks through electrode interfacial redox reactions. For instance, Zhang's group[15] at Tsinghua University developed quantum dot gels with 3D networks via electrochemical ligand

[1]Suzhou Institute of Nano-tech and Nano-bionics, Chinese Academy of Sciences, Suzhou, PR China. [2]School of Textile Science and Engineering, Jiangnan University, Wuxi, PR China. e-mail: xtzhang2013@sinano.ac.cn

removal and disulfide crosslinking. Nevertheless, the development of electrochemical gelation remains constrained by its reliance on specific redox systems. The strategic combination of electrophoretic assembly and electrochemical gelation presents a promising yet unexplored approach for simultaneous control over colloidal migration, assembly, and network formation.

Aramid nanofibers (ANFs), inheriting exceptional properties from their parent fibers (one of three major high-performance fibers), exhibit remarkable attributes including low density, ultrahigh strength-to-weight ratio, excellent thermal stability, and desirable chemical resistance. These aramid nanofibers obtained through alkaline/DMSO exfoliation of Kevlar fibers carry substantial negative surface charges, named aramid colloidal particles[16–19]. Professor Nicholas A. Kotov's team from the university of Michigan[16] pioneered the exploration of stripping aramid fibers in a KOH/DMSO environment to obtain ANF dispersion in 2011. Based on this, researchers have continuously proposed some efficient methods for the preparation of ANF. Zhang et al.[17] adopted a proton donor-assisted aramid deprotonation strategy, reducing the preparation time of ANFs from the traditional 7 days to 4 hours. Recently, Yu et al.[18] adopted the molecular intercalation method to reduce the preparation time of ANFs to 4 min. Based on the innovation of microfluidic engineering, our group[19] proposed a efficient method for the continuous preparation of aramid colloid dispersions. By precisely regulating the hydrodynamic parameters, a dual improvement in process efficiency and product uniformity was achieved. The unique characteristics[20–24] of ANFs might offer three key advantages for electric-manipulation in aramid colloidal aerogel fabrication including enhanced electrophoretic mobility due to high surface charge density, facilitated orientation control via anisotropic fibrous morphology, and triggered electrochemical gelation by electrolytic proton generation. Despite extensive progress on ANF applications[25–30], including composite reinforcement, battery diaphragm and advanced aerogels[31–35], the fundamental understanding and practical electro-manipulating implementation of negative charged aramid nanofibers for colloidal aerogel films remain uncharted territory.

Herein, electro-manipulation of negative-charged aramid nanofibers was proposed and successfully employed to fabricate micro-/macro-scale colloidal aerogel films with precisely hierarchical structures and enhanced performance. Initially, negative-charged ANFs were prepared through alkali stripping of Kevlar fibers. Subsequently, the movement, orientation, and gelation process of negative-charged ANFs were precisely regulated through the integration of electrophoretic and electrochemical techniques, resulting in the fabrication of thin colloidal aerogel films with controlled nanofiber alignment. These films exhibited superior mechanical strength, good thermal insulation property, and excellent proton transport performance compared to conventional aerogel films. Additionally, the high precision and efficiency of electro-manipulation render it advantageous for both microscale regulation and large-scale engineering production of ANF aerogel films. By combining the desirable properties of aerogels with tailored microstructure design, this approach holds great promise for the engineering-scale production of high-performance functional aerogel films (e.g., oil-water separation films). The external field regulation strategy presented here provides theoretical guidance and technical support for achieving structural-performance control in aerogels (Fig. 1).

Results

Electro-manipulating of negative-charged aramid nanofibers

The negative-charged ANFs colloidal dispersion were firstly fabricated by dispersing Kevlar fiber in KOH/DMSO solution as reported previously[16]. Through the application of a direct current electricity to the ANFs dispersion, it was observed that gels continuously formed at the anode, accompanied by a gradual change in the solution's color from red to light yellow, ultimately becoming clear and transparent (Supplementary Figs. 1, 2). This phenomenon indicates the continuous electrophoretic movement of negative-charged ANFs towards the anode under the influence of an applied electric field (Fig. 2a). The relationships between gel thickness and the duration of electrical processing with different dispersion concentrations and electric field strengths were investigated (Supplementary Fig. 3). Specially, in an 0.2 wt% ANFs colloidal dispersion, the film thickness exhibited a progressive increase with prolonged electric treatment time. Furthermore, the gel thickness demonstrated a direct correlation with the applied electric field strength, where higher electric field strength accelerated the growth rate of the gel thickness (Fig.2b). Based on the experimental data in Fig. 2b, we calculated the migration speeds of the nanofibers under varying electric field intensity, as depicted in Fig. 2c. As the electric field intensity increases from 4 V/cm to 10 V/cm, the migration rate of the nanofibers escalates from 2.0×10^{-7} m s^{-1} to 1.2×10^{-5} m s^{-1}, demonstrating that the speed of the nanofibers can be modulated by adjusting the applied voltage. By the way, power cuts do not impair the gel's growth ability, it can continue growing after power is reconnected (Supplementary Fig. 4).

To further investigate the electrophoretic assembly of ANFs, the orientation of the generated ANFs gel can be visually monitored through a polarizing microscope (Fig. 2d, Supplementary Fig. 5). At lower voltages, no significant birefringence is evident in the gel film. However, as the voltage increases, the birefringence phenomenon becomes increasingly apparent (Fig. 2e). By rotating the sample, a transition from light to dark can be observed, indicative of the layered structure's orientation. The formation of layered structures can be described as a multi-step process involving anchoring and orientation. Initially, the ANFs migrate and anchor to anode through electrophoresis of ANFs. Under low electric field intensity, the electrostatic force

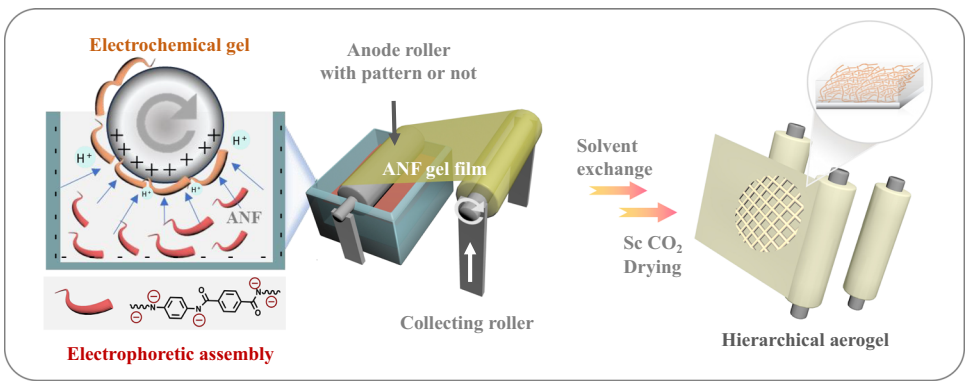

Fig. 1 | Schematic illustration on electro-manipulating of negative-charged aramid nanofibers towards micro-/macro-scale colloidal aerogel films. ANF aramid nanofiber.

https://doi.org/10.1038/s41467-025-63827-y

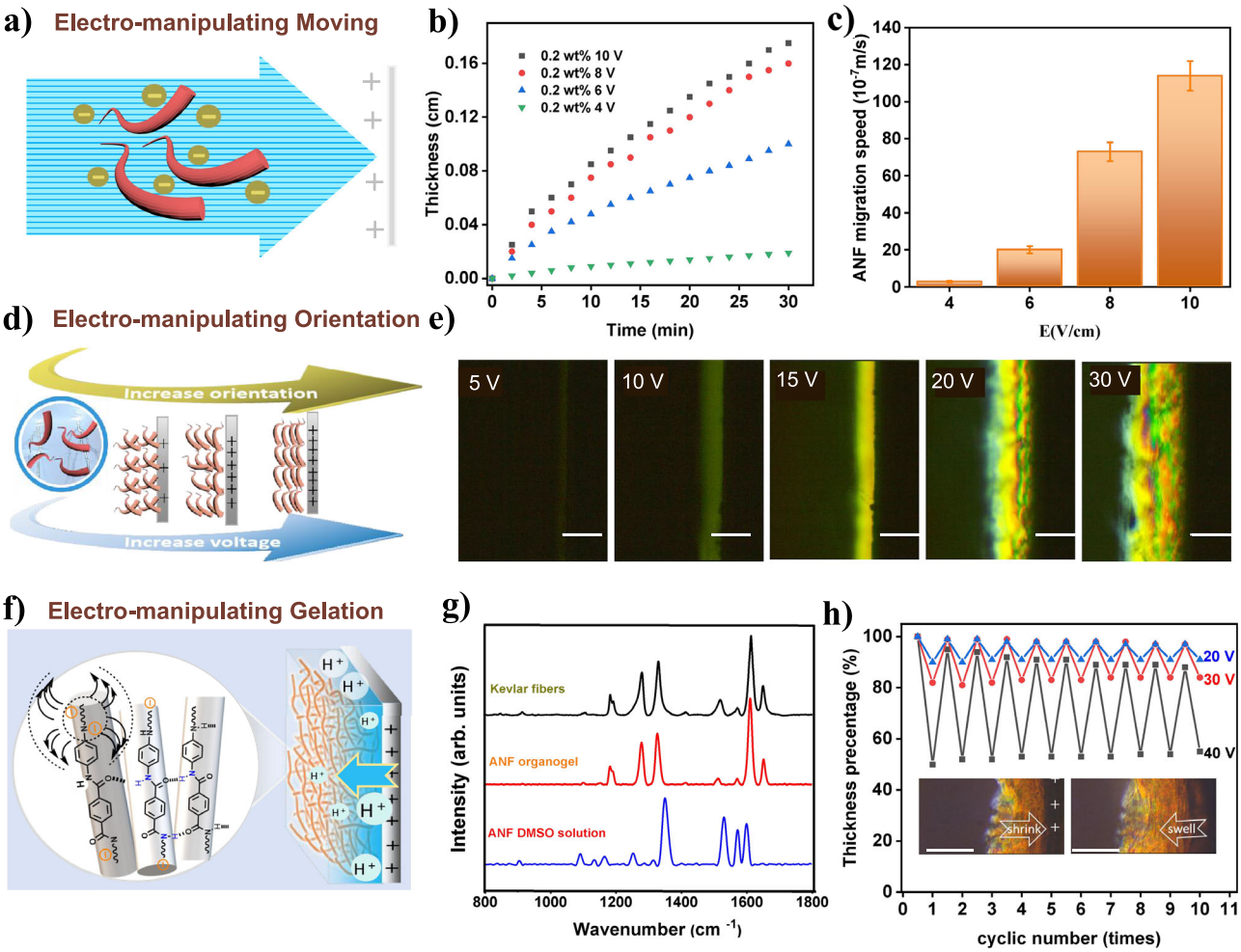

Fig. 2 | Electro-manipulating behaviors of negative-charged aramid nanofibers. **a** Schematic illustration showing electro-manipulating movement of aramid nanofibers. **b** Thickness of aramid colloidal gels as functions of electromigration time. **c** Electromigration velocity of nanofibers. ANF: aramid nanofiber. Data are presented as mean ± SD ($n = 3$ independent experiments) **d** Schematic illustration on electro-manipulating orientation of nanofibers. **e** Polarizing microscope images of nanofibers with different orientations, scale bar: 200 μm. **f** Schematic illustration on electrochemical gelation of aramid nanofibers. **g** Raman spectrum of aramid nanofiber and ANF gel. **h** shrinking and swelling of aramid nanofiber gel during switching on/off different voltages, inset scale bar: 500 μm.

acting on ANFs is relatively weak, thereby failing to provide sufficient driving force to overcome their inherent resistance, including steric hindrance and electrostatic repulsion. Consequently, this resistance restricts the further movement and alignment of ANFs on the anode surface, leading to a lower degree of ANFs orientation. In contrast, when subjected to higher electric field strength, the enhanced electrostatic attraction surpasses the resistive forces, facilitating the layer-by-layer alignment of ANFs toward the anode and promoting a higher degree of orientation.

In contrast to conventional electrophoretic deposition processes that typically yield dense films, a distinctive feature of this method is its ability to produce ANF gel structure[36]. Typically, the sol-gel transition of aramid nanofibers (ANFs) necessitates the incorporation of additional chemical cross-linking agents, such as water, acids, esters, or metal ion cross-linkers[20–24]. Surprisingly, in our work, sol-gel transition occurred without the addition of any cross-linking agents beyond the application of electricity. To elucidate the underlying mechanisms, we conducted comprehensive investigations into both the chemical pathways and kinetic processes governing gel formation. Firstly, the chemical structure of the dried gel film was analyzed. The infrared spectrum of the film was identical to that of Kevlar fibers, indicating that the gel network was solely composed of ANFs without any other chemical components (Supplementary Fig. 6). Furthermore, the reversible dissolution of the gel and dried films in base indicates that the nanofibers are held together by non-covalent interactions (physical cross-linking) rather than permanent covalent cross-links. (Supplementary Fig. 7). Therefore, the sol-gel transition of the ANF colloid was attributed to the reprotonation of negatively charged ANFs rather than anodic oxidation.

To explain the reprotonation process of ANFs at the anode, the pH values at different regions and electrochemical products at the anode and cathode were tested. The results showed that the pH near the anode was close to 7, indicating a significant reduction in alkalinity in that vicinity. Through systematic analysis of electrochemical products at both electrodes combined with in situ pH monitoring, we established that DMSO undergoes anodic decomposition under applied potential, generating H^+ ions (Supplementary Figs. 8–11, Supplementary Note 1, 2). These protons subsequently react with negatively charged ANFs in the anode vicinity, inducing their reprotonation (Fig. 2f) and ultimately driving the sol-gel transition. Raman spectroscopy directly confirmed the reprotonation process during the sol-gel transition. The Raman spectrum of pristine Kevlar fibers matched previously reported profiles. Upon dispersion in KOH/DMSO, the negatively charged ANFs exhibited significant spectral changes in the 800–1800 cm^{-1} range, consistent with deprotonation. However, during gel formation at the anode, the spectra reverted to nearly identical

profiles to those of pristine Kevlar fibers, confirming the reprotonation of ANFs (Fig. 2g). Collectively, our findings establish that the electrochemical gelation originates from DMSO decomposition at the anode, with the resulting protons induced reprotonation of negatively charged ANFs.

Therefore, electro-manipulating of negative-charged aramid nanofibers involves complex kinetic processes, including the electrophoresis movement, orientation of negative-charged ANFs and the electrochemical sol-gel transition. During the application of direct electricity, negatively charged nanofibers accumulate at the anode under the attraction of an electric field. Simultaneously, H^+ ions generated at the anode diffuse towards the ANFs, reacting with N^- on ANFs to form amide bonds (Supplementary Fig. 12). These amide bonds, along with π-π interactions between phenyl rings, form physical cross-linking points, resulting in a three-dimensional cross-linked network. The sol-gel transition remains incomplete during early-stage nanofiber accumulation at the anode, as un-reprotonated fiber surfaces retain negative charges that generate inter-fiber repulsive forces. As evidenced in Fig. 2h and Supplementary Fig. 13, Movie 1, upon cessation of the electric field, the formed gel film swells due to repulsive forces between the nanofibers. When the voltage is reapplied, the negatively charged gel network contracts toward the anode, exhibiting thickness shrinkage of 10%, 20%, and 50% under electric field intensities of 20 V/cm, 30 V/cm, and 50 V/cm, respectively. These observations collectively explain the formation mechanism: the balance between partial re-protonation-induced attraction and residual charge repulsion favors three-dimensional gel network formation over dense film compaction.

Unlike in aqueous systems, during the electrochemical process, the anode neither produces gases that disrupt the gel film structure nor generates metal ions that contaminate the ANF gel. This is a crucial prerequisite for the subsequent preparation of high-performance pure aramid nanofiber aerogels with precise structures. The migration speed of nanofibers, the diffusion rate of gelation factors, and the gelation speed of nanofibers jointly contribute to the formation of partially reprotonated aramid nanofiber gel networks. The negative charges within the gel network prevent the dense packing of nanofibers, ensuring a mesoporous structure in the aerogel, while simultaneously enabling orientation control of the nanofibers.

Nanofiber network regulation and performance enhancement

The electro-manipulated gel film was subsequently immersed in ethanol to facilitate the complete reprotonation of ANFs and to remove residual DMSO and electrolyte. After thorough solvent exchange with ethanol and drying under supercritical CO_2 (Sc CO_2) conditions, the wet gel was successfully transformed into an aramid colloidal aerogel, hereafter referred to as electro-manipulated aramid colloidal aerogel (EM-AC aerogel). Initially, the chemical and microstructural characteristics of EM-AC aerogel were investigated. Based on the analysis of infrared spectroscopy and Raman spectroscopy (Fig. 2g, Supplementary Fig. 6), it can be concluded that the chemical composition of the aerogel is identical to that of pure aramid fibers. The X-ray diffraction (XRD) pattern (Supplementary Fig. 14) exhibited prominent diffraction peaks at specific 2θ angles of 20°, 23°, and 28°, which can be attributed to the (110), (200), and (004) reflections, respectively. These peaks are in accordance with those observed in aramid fibers, suggesting that the crystalline structure of the nanofibers remained unaltered during the electro-manipulation process. Thermogravimetric analysis (TGA) of the EM-AC aerogel film was shown in Supplementary Fig. 15, Before 300 °C, slight weight loss was observed, attributed to the desorption of adsorbed water molecules. As the temperature further increased to 565 °C, the film exhibited a significant weight loss, similar to pure Kevlar fiber, underscoring the high purity of the aramid colloidal aerogel and its high thermal stability. As shown in inset of Fig. 3a, the isotherm of all samples exhibits a rapid increase in the low-pressure range and a hysteresis loop, indicating the existence of micropores and mesopores, with the specific surface area of 234 m^2/g and pore size of 12 nm, respectively (Fig. 3a, Supplementary Fig. 16).

Scanning electron microscopy (SEM) was employed to investigate the internal microstructures of EM-AC aerogel films with densities ranging from 21.2 mg cm^{-3} (porosity: 98.5%) to 112.1 mg cm^{-3} (porosity: 92.2%) tuning by applied voltage. From the side view, the films exhibited a distinct layered stacking architecture, with each layer comprising an interwoven three-dimensional network of aramid nanofibers. As the density increased, the layered structure became more distinct, reflecting tighter packing and enhanced structural integrity (Fig. 3b). Unlike the macroporous aerogel prepared by bidirectional freezing, the layered structure here still maintains mesoporous attribute[37]. In contrast, the top view revealed a disordered yet interconnected three-dimensional nanofiber network, characteristic of the aerogel's porous framework. With increasing density, the pore size within the network gradually decreased, indicating a denser and more compact morphology (Supplementary Fig. 17). Furthermore, the orientation degrees of EM-AC aerogel films from side and top view were measured using two-dimensional XRD. From the side view, the orientation of the nanofibers within the EM-AC aerogel films was analyzed as a function of density. At a density of 21.2 mg cm^{-3}, the diffraction peak intensity was relatively low, corresponding to an orientation value of approximately 0.15. As the density increased to 69.8 mg cm^{-3}, the diffraction peak intensity became more pronounced, with the calculated orientation rising to about 0.37. Further increasing the density to 112.1 mg cm^{-3} resulted in even stronger diffraction peaks and an orientation value of approximately 0.46. These findings demonstrate a clear trend: higher surface densities correlate with increased nanofiber orientation (Fig. 3c, d). From the top, the diffraction peak intensity is weak, and the orientation is almost 0. These findings were consistent with the observations from SEM and polarized light microscopy, indicating that increasing the electric field intensity significantly enhanced the orientation of the layered structure in the aerogel.

The properties of the colloidal aerogels are intrinsically tied to their chemical composition and internal structure. The EM-AC aerogel, which is exclusively composed of pure aramid nanofibers connected by non-covalent bonds like hydrogen bonds. The physically cross-linked aerogel can be readily redispersed in strongly alkaline/DMSO solution to reform an ANF dispersion, allowing electrochemical gelation again and demonstrating excellent recyclability (Supplementary Fig. 18a). Moreover, the aramid aerogel not only inherits the high-temperature and solvent resistance of aramid materials but also exhibits the characteristic thermal insulation, low dielectric constant properties, and self-extinguishing flame retardancy typically associated with aerogels (Supplementary Figs. 18–21). Although aramid aerogels are inherently not water-resistant, they could gain hydrophobic properties after fluorocarbon resin treatment[38] (Supplementary Fig. 21a).These attributes make it suitable for diverse applications reported elsewhere[31–35], including thermal insulation, separation, and infrared stealth. The EM-AC aerogel's lamellar structure endows it with distinct physicochemical properties, including mechanical strength, thermal insulation, and ion transport. Unlike conventional isotropic aerogels, the EM-AC aerogel exhibits disordered nanofibers orientation in the transverse and longitudinal direction, while highly aligned nanofibers parallel to the film plane, resulting in superior in-plane mechanical performance. The 115.6 mg cm^{-3} EM-AC aerogel showed nearly identical high tensile moduli in longitudinal (200 MPa) and transverse (199 MPa) directions, attributable to the disordered fiber alignment along these axes (Supplementary Fig. 22). A comparative analysis of tensile strength between the EM-AC aerogel film and an aramid colloidal aerogel film prepared by traditional blade coating method (BC-AC aerogel) both at 112 mg cm^{-3} revealed that the former

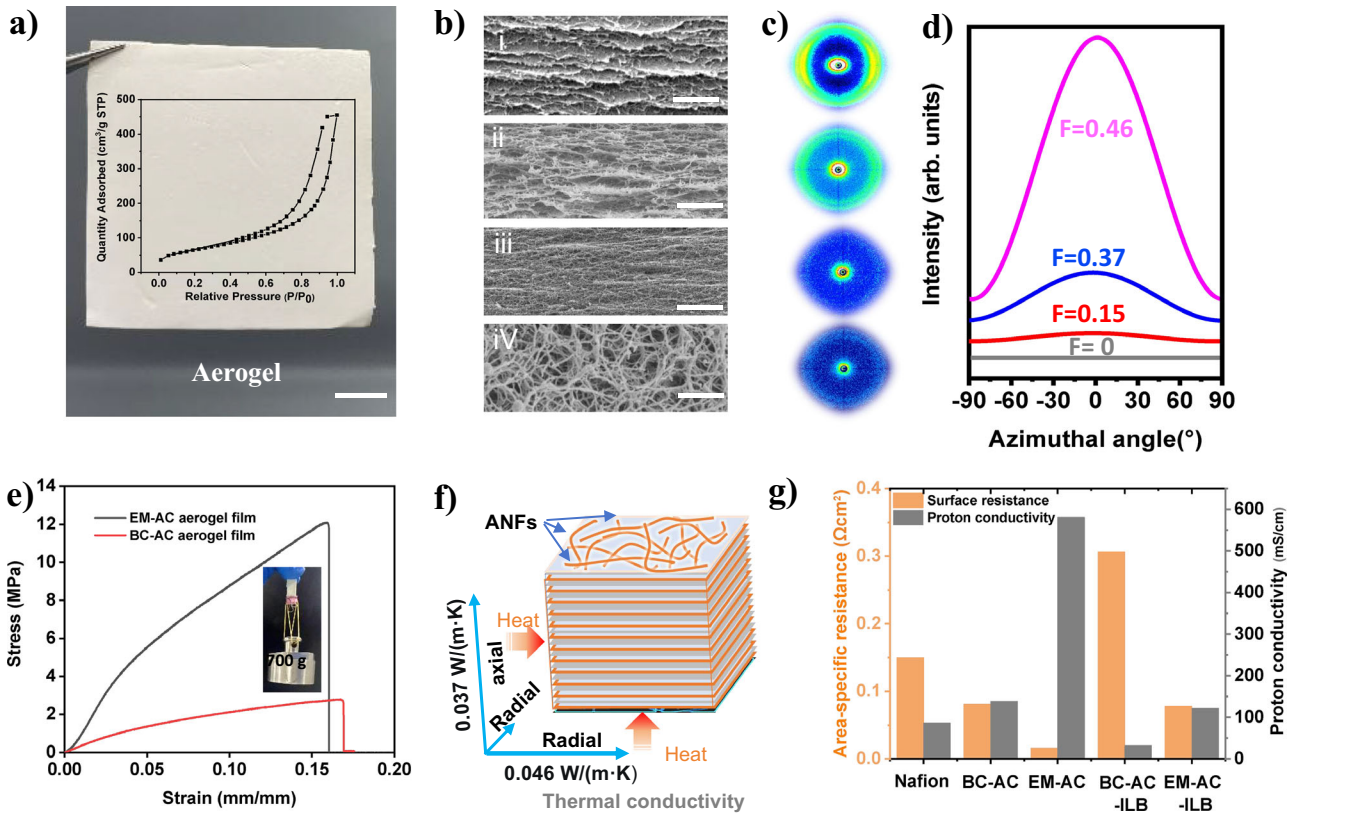

Fig. 3 | Structures and properties of EM-AC aerogel. a Optical photo of aramid colloidal aerogel film prepared by EM strategy (scale bar, 1 cm) (Inset: nitrogen adsorption-desorption curve of the resulting aerogel film with density of 69.8 mg cm^{-3}. **b** SEM images (scale bar, 1 μm), **c** typical WAXS patterns and **d** its relative radial profiles from the side cross-section views of ANF aerogel films with densities varying from (i) 21.2 mg cm^{-3}, (ii) 69.8 mg cm^{-3} and (iii) 112.1 mg cm^{-3} and from iv) top view of ANF film. **e** Stress-strain curves of the electro-manipulated aramid colloidal (EM-AC) aerogel films and blade-coating aramid colloidal (BC-AC) aerogel films with density of 112 mg cm^{-3}. **f** Parallel and vertical thermal conductivity of EM-AC aerogel film with density of 69.8 mg cm^{-3}. **g** Area-specific resistance and proton conductivity of different films including commercial Nafion film, BC-AC, EM-AC aerogel film (48.5 mg cm^{-3}), the BC-AC and EM-AC aerogel film with ionic liquids (BC-AC-ILB, EM-AC-ILB).

achieved a fracture strength of up to 12 MPa—approximately five times greater than that of the latter. Remarkably, an EM-AC aerogel film with a width of 1 cm and a thickness of about 500 micrometers could suspend a weight of 700 g, equivalent to 10,000 times its own weight (Fig. 3e). Additionally, the aerogel film demonstrated excellent flexibility, maintaining structural integrity without cracking even after reiterative origami (Supplementary Fig. 23).

The anisotropic microstructure also accounts for the directional thermal conductivity difference. The aerogel's total thermal conductivity (λ_{total}) in air comprises three components: solid-phase conduction (λ_s), gas-phase conduction (λ_g), and radiative transfer (λ_r), where λ_r is negligible at room temperature. The anisotropic lamellar structure preferentially facilitates radial heat transfer through the solid phase while restricting both λ_s and λ_g in the axial direction, resulting in higher radial λ_s compared to axial λ_s. Figure 3f displays the thermal conductivity of 69.8 mg cm^{-3} EM-AC aerogel in the axial and radial directions, along with a schematic diagram illustrating heat transfer in both directions at 25 °C. The radial thermal conductivity was 0.046 W/(m·K), and the axial thermal conductivity was 0.037 W/(m·K) at 25 °C (Fig. 3f). Compared with axial conductivity of unoriented BC-AC aerogel with similar density (0.042 W/(m·K)), layered oriented EM-AC aerogel show better thermal insulation performance. COMSOL finite element simulation of thermal conductivity of isotropic BC-AC aerogel film and anisotropic EM-AC verified the similar conclusion. (Supplementary Fig. 24).

Additionally, we investigated the ion transport behavior of aramid colloidal aerogel films. The proton conductivities of commercial Nafion, conventional BC-AC aerogel, and EM-AC aerogel films (all ~100 μm thick) were 87, 139, and 581 mS/cm², respectively. Therefore, compared to conventional aerogel film and commercial Nafion film, EM-AC aerogel film exhibited faster proton transport rates. When the EM-AC aerogel film was combined with ionic liquids (EM-AC-ILB) for potential application in vanadium flow battery separator, EM-AC-ILB film maintain vanadium resistance for over 7 days, while commercial Nafion film (N115) maintain that less than 12 h (Supplementary Fig. 25). Besides, EM-AC-ILB film not only exhibited higher vanadium permeation resistance but also faster proton transport performance with 86.7 mS/cm², 64.1 mS/cm² and 121.7 mS/cm² for Nafion, BC-AC-ILB, and EM-AC-ILB, respectively. (Fig. 3g).

Conformal microstructure construction with broader application

Nature achieves unique functionalities through hierarchical micro/nano-porous structures, as exemplified by spider silk's oriented nanofibers and micron-scale spindle knots together enabling efficient water harvesting[39]. However, conventional sol-gel methods for aramid aerogels face challenges in constructing such multiscale architectures due to high viscosity and poor fluidity of aramid dispersions, which impede microsurface penetration and conformal coating (Supplementary Fig. 26). In contrast, EM strategy effectively overcomes these issues: firstly, ultra-dilute (≥0.01 wt%), low-viscosity dispersions enabling facile microsurface infiltration; then, an in-situ gradual sol-gel transition permitting conformal microsurface growth; These advantages facilitate the formation of conformal aramid gel films on

https://doi.org/10.1038/s41467-025-63827-y

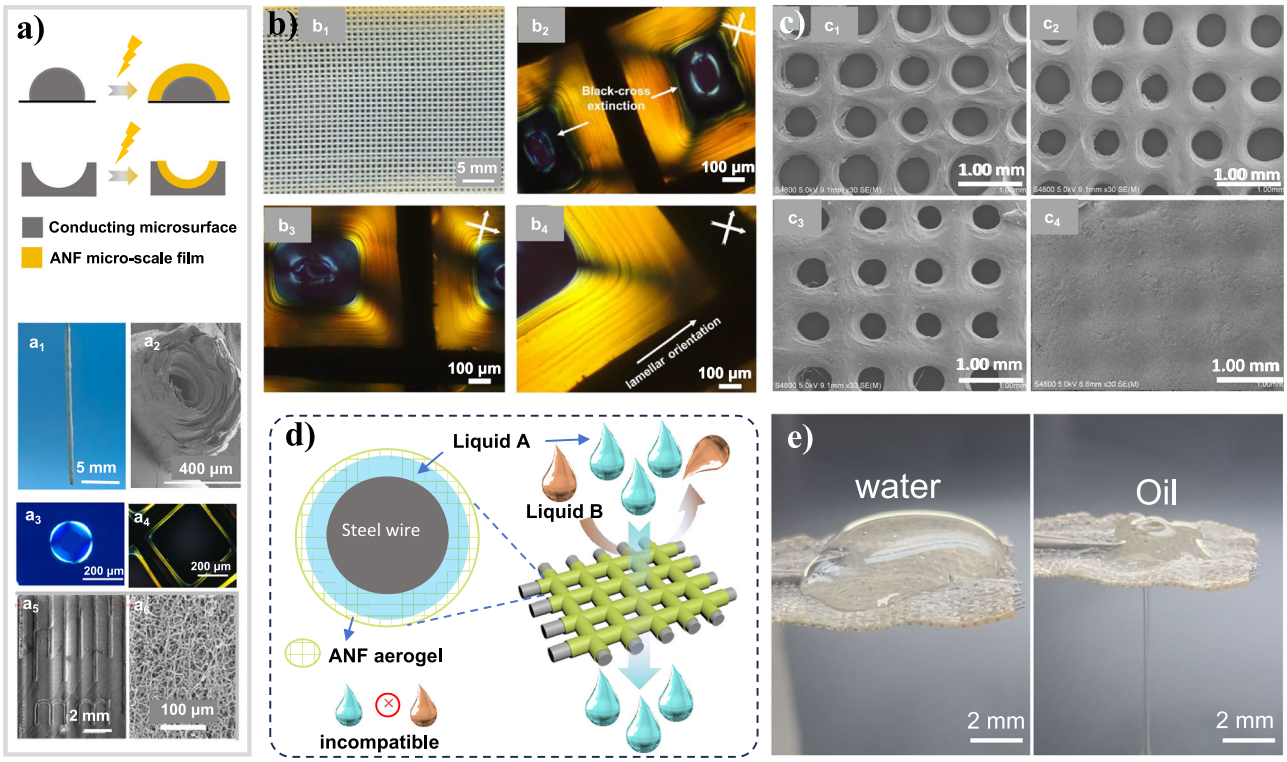

Fig. 4 | Conformal colloidal aerogels on conductive microsurfaces via EM strategy. a Schematic diagram on fabrication of ANF aerogel on the conductive microsurfaces. $\mathbf{a_1}$, $\mathbf{a_2}$ aerogel on the surface of fine stainless steel needle. $\mathbf{a_3}$, $\mathbf{a_4}$ aerogel on the microporous surface. $\mathbf{a_5}$, a_6 aerogel on the surface with micro patterns. ANF: aramid nanofiber. **b** Photo and POM images of the colloidal aerogels on stainless steel mesh. **c** SEM images of conformal colloidal aerogel meshes with different pore sizes. **d** Application illustration of aerogel mesh for self-replenishing liquid separation. **e** Application demonstration of oil-water separation by aerogel mesh.

conductive microsurfaces, as illustrated in Fig. 4a. Conformal sol-gel transition on microstructured surfaces (e.g., needles, pores, and patterned substrates), followed by Sc CO_2 drying, produce colloidal aerogel shells with three-dimensional porous nano-network architecture (Supplementary Figs. 27–29). For instance, when 100 μm thick stainless steel needles serve as conductive substrates, they yield 400 μm concentric colloidal aerogel fibers (Fig. 4a_1, a_2). Similarly, using round holes with a diameter of 200 μm and square holes with a width of 400 μm as conductive substrates facilitate the formation of micro-aerogel hollow films, where the bright areas in the polarizing microscope represent the formed conformal gel. (Fig. 4a_3, a_4). What is more, patterned conductive steel rulers transfer their designs onto the aerogel surface, where the enlarged scale reveals a crisscrossed network of aramid nanofibers. (Fig. 4a_5, a_6). Figure 4b illustrates the conformal colloidal aerogel on the more complex array structures like mesh. Under polarized light microscopy, it is evident that the stainless steel mesh is uniformly coated with oriented aramid colloidal aerogel (Fig. 4b). The size of the conformal aerogel pores and the wrapping configuration can be precisely regulated by adjusting the electric field strength and power-on time. The diameters of the pores range from approximately 500 μm, to 300 μm, to 250 μm, and to completely closed pores, under an electric field intensity of 20 V/cm with different electrification times (1 min, 3 min, 5 min, 20 min). (Fig. 4c).

The precisely engineered micro-nano structures achieved through conformal sol-gel transition significantly enhance the performance of aramid colloidal aerogel films, enable functional properties and broaden their potential applications. For instance, cold-end temperatures of patterned-EM-AC aerogel, EM-AC aerogel and traditional BC-AC aerogel on 60 °C heating stage were 57.4 °C, 58.1 °C, 58.5 °C, respectively, indicating that patterned-EM-AC aerogel with micro-nano structures display best thermal insulation (Supplementary Fig. 30). Another example, conformal aerogels on stainless steel meshes can form core-shell aerogel networks. The micropores of the conformal mesh provide efficient pathways for rapid mass transport, while the nanoscale network of the aerogel imparts multifunctional properties, such as thermal insulation, adsorption, limited functional guest accommodation, and supported catalysis[40]. As a demonstration of its application in separation, pre-filling one component of a mixture into the aerogel network enables the efficient separation of two immiscible components (Fig. 4d). For example, pre-filling the aerogel network with oil allows selective oil permeation while effectively blocking water (Fig. 4e).

Beyond leveraging the micro-nano architecture of aerogels, integrating substrate properties can further enhance aerogel performance. The conformal aerogel on stainless steel mesh inherits the high mechanical properties of the substrate, enabling repeated shape manipulation without significant structural failure (Supplementary Fig. 31). Notably, a 1 cm-wide steel mesh conformal aerogel can effortlessly lift a 1 kg load without fracture, while demonstrating remarkable resistance to high-speed water impact and sharp needle penetration. These superior mechanical properties ensure reliable operation of conformal aerogels under harsh real-world conditions. The transportation, drilling, or accidental leakage of high-viscosity crude oil presents a global environmental challenge. By synergizing the electrothermal/ electromagnetic induction heating capability of stainless steel mesh with the oil-water separation characteristics, the fluidity of viscous oil can be significantly improved to facilitate separation and recovery[41]. As shown in Supplementary Fig. 32, viscous oil adheres to the mesh with limited mobility at 25 °C, while heating above 80 °C rapidly reduces oil viscosity enabling efficient separation. Furthermore, additional properties of stainless steel (e.g., ferromagnetism) can be exploited to design magnetically responsive

https://doi.org/10.1038/s41467-025-63827-y

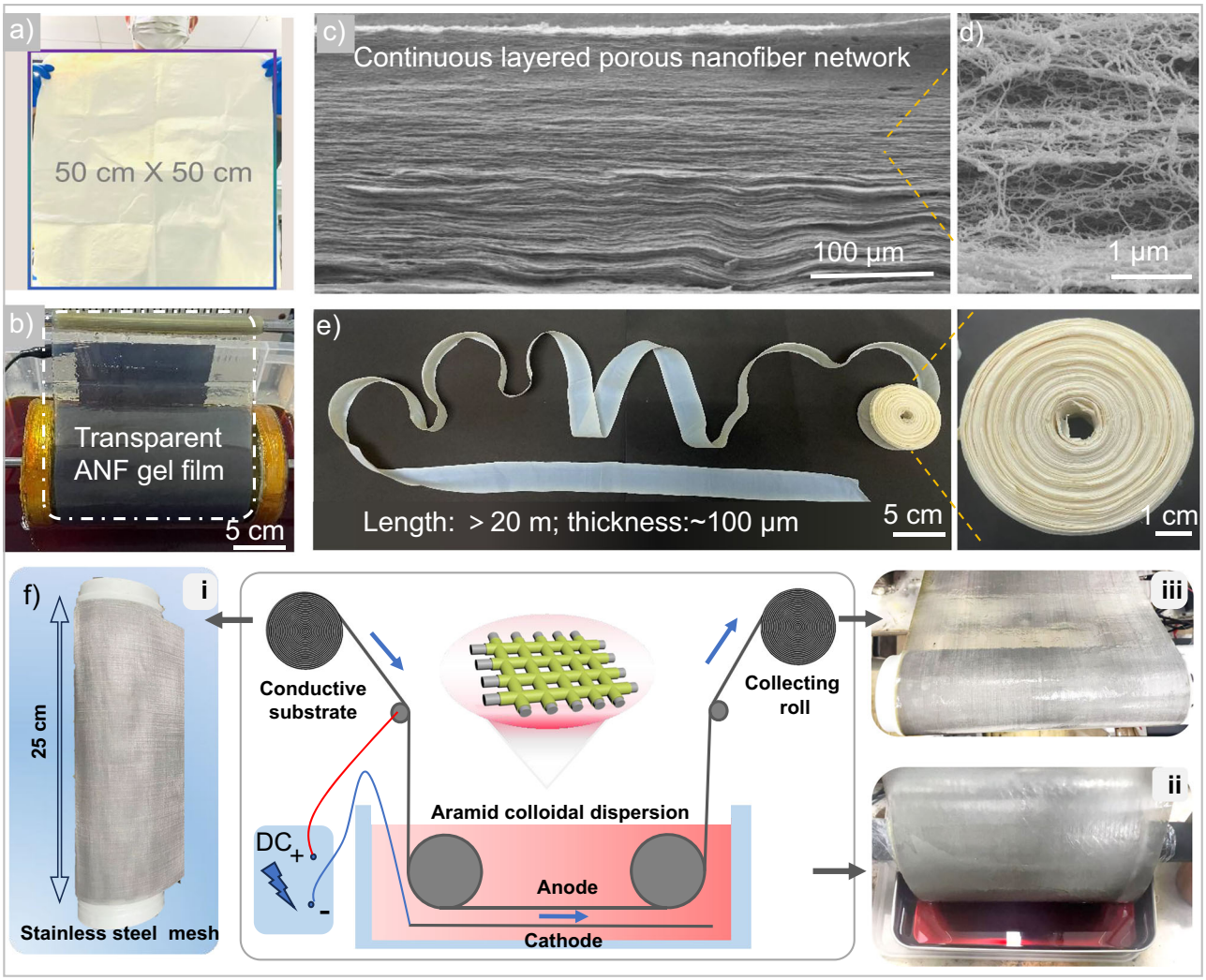

Fig. 5 | Large-size, continuous aramid aerogels prepared by EM strategy. **a** Photos of large-size (50 × 50 cm) free-standing aramid colloidal aerogel films with density of 52.6 mg cm^{-3}. **b** Photos of free-standing roll-to-roll gel film device. ANF: aramid nanofiber. **c** SEM images of roll-to-roll layered aramid colloidal aerogel films. **d** Amplified SEM images. **e** Continuous aramid colloidal aerogel film with density of 48.5 mg cm^{-3} over 20 m in length and approximately 100 μm in thickness. **f** Diagram of roll-to-roll preparation of EM conformal aramid colliodal gel films on conductive films with microstructures. (i) conductive stainless steel coil, (ii) EM conformal sol-gel transition, (iii) collection of conformal aramid colliodal gel films.

conformal aerogels. In brief, rational micro-nano structural design coupled with tailored physicochemical properties of both aerogels and substrates provides an effective strategy to enhance aerogel performance and expand their application frontiers.

Large-area, continuous fabrication of aramid colloidal aerogels

Aerogel films with micro and nano structures can play an important role, but to achieve the transition from laboratory to practical application, it is necessary to solve the problem of large-area as well as continuous fabrications. During the large-aera fabrication of aerogel films, conventional methods such as blade coating often result in non-uniform sol coating, inconsistent gelation, and uneven shrinkage. These issues lead to defects like cracking, wrinkling, and thickness variation, making it challenging to produce high-quality, large-area aerogel films (Supplementary Fig. 33a). Moreover, these methods struggle to precisely control the aerogel's micro- and nanostructures. As a result, there are few reports on fabrication of uniform, large-area, self-supporting aramid aerogel films. In contrast, the EM strategy offers a promising solution, allowing the fabrication of large-area aramid colloidal aerogel films simply by using conductive substrates as the base (Supplementary Fig. 33b). As demonstrated in Fig. 5a, the EM approach has successfully produced uniform free-standing aerogel films with dimensions up to 50 × 50 cm. The successful formation of ANF gel films on both curved substrates (Supplementary Fig. 34) and electrically modified insulating substrates (Supplementary Fig. 35) further demonstrates the flexible adaptability of the EM strategy for complex operational conditions.

In addition, the continuous fabrication of aramid colloidal aerogel films can be achieved through the design of the anode. By employing a continuously circulating conductive substrate as the anode, this system enables the continuous production of aerogel films. As illustrated in Fig. 1, the setup consists of five key components: an ANF (aramid nanofiber) dispersion bath, an anode circular roller, a stationary cathode plate, a film-collecting roller, and a direct current power supply. Under direct current, ANFs (aramid nanofibers) continuously migrate onto the rotating anode roller surface, forming a uniform colloidal gel film. As the roller rotates, the gel film emerges from the liquid interface, where it is peeled off and transferred to the collecting roller. Simultaneously, the newly immersed roller section initiates the formation of a fresh gel layer, establishing a continuous production cycle for aramid gel films. The film formation device, stripping and collecting of wet film are illustrated in Fig. 5b, with the actual film

formation process captured in Supplementary Movie 2. Initially, the wet gel film displays high transparency (91% transmittance at 600 nm), which evolves into a translucent morphology (70% transmittance at 600 nm) after solvent exchange in ethanol and Sc CO_2 drying, yielding a robust free-standing aramid colloidal aerogel film with a width of ~20 cm (Supplementary Figs. 36, 37).

The continuous fabrication of aramid colloidal aerogel films enables precise control over their macro/micro/nano-scale structures. By precisely adjusting process parameters, aerogel films with customizable properties, including tunable widths and optical transparencies, can be fabricated (Supplementary Fig. 38). By engineering micropatterns onto the anode roller, we demonstrate the continuous production of aerogel films with designed microarchitectures (Supplementary Fig. 39), underscoring the high versatility of this approach. Simultaneously, the EM strategy facilitates continuous production of aerogel films with orientation-controllable nanofiber network architectures, a capability unattainable through conventional methodologies. For instance, Fig. 5c, d shows a continuous layered porous aramid colloidal aerogel. Remarkably, this approach enables the fabrication of aramid colloid aerogel films with continuous lengths exceeding 20 meters (Fig. 5e), demonstrate the engineering potential of this method.

Beyond free-standing films, this platform technology extends to the continuous preparation of conformal aerogel composites on diverse micro-substrates. As depicted in Fig. 5f, 25 cm wide stainless steel mesh is continuously permeated with an ANF dispersion. Subsequently, under direct current, stainless steel mesh acts as anode, and conformal gel film on the stainless steel mesh generated via electrochemical sol-gel transition of ANF colloid. The resulting conformal gel film is collected using a collection roller and further processed to obtain conformal aerogel with hierarchical structures after drying (Supplementary Fig. 40). Thus, the large-size, continuous fabrication of aramid colloidal aerogels with macro/micro/nano-structures via EM strategy, combined with the special properties exhibited by these hierarchical structures, are expected to advance the engineering applications of precisely structural aerogel films.

Discussion

In this study, we introduce and demonstrate an innovative electromanipulation strategy for fabricating micro- and macro-scale colloidal aerogel films from negative-charged aramid nanofibers (ANFs). By electrophoresis assembly and electrochemical reactions, we precisely regulate the movement, orientation, and gelation of ANFs, enabling the formation of hierarchical structures with enhanced functionalities. After solvent exchange and supercritical CO_2 drying in sequence, the resulting ANFs aerogels retain the intrinsic properties of pure aramid fibers, including high-temperature resistance, solvent resistance, crystallinity, and recyclability. In addition, the EM strategy endows this work with stronger multi-scale structural regulation capabilities, performance enhancement and application expansion. Firstly, the electrically-controlled oriented nanofiber structure further enhances mechanical properties, thermal insulation, and proton transport rate. Then, this EM strategy offers high precision, making it suitable for microscale adjustments. By combining the functional properties of aerogels with tailored microstructural designs, this approach holds significant promise for various applications, such as thermal management and oil-water separation. Finally, the scalability of this EM strategy enables the large-scale continuous production of aramid aerogels with the above micro-nano structures, demonstrating engineering potential. The proposed external field regulation strategy provides a robust theoretical and technical framework for achieving structural-performance control in aerogel manufacturing. Moving forward, further studies could investigate the use of external fields (e.g., optical, magnetic, and acoustic) as stimuli to guide the assembly and sol-gel transition of colloidal nanoparticles with tunable shapes and properties, enabling the fabrication of aerogels with tailored micro-nano architectures. Concurrently, it will be essential to develop robust quantitative methods to describe these microstructural features and establish deeper structure-property correlations[42]. By combining computational modeling with experimental validation, we can expedite the design and optimization of aerogels for diverse functional applications.

Methods

Materials

Kevlar 1000D was purchased from DuPont Company, Potassium hydroxide (KOH, ≥99.95%) was obtained from Shanghai Aladdin Biochemical Technology Co, Ltd. Potassium tert-butoxide (t-BuOK, 99%), Dimethyl sulfoxide (DMSO, ≥99.5%) was obtained from China National Pharmaceutical Group Co., Ltd. (Sinopharm). Ethyl alcohol (99%) was obtained from Suzhou Jingxie High and New Electronic Material Co., Ltd. Deionized water (18.2 MΩ cm-1) was obtained from a Millipore-Q system. All other reagents were used without further purification.

Preparation of Kevlar nanofiber solution

Kevlar 1000D was dissolved in KOH/t-BuOK DMSO to obtain a dark red solution of aramid nanofibers (ANFs), which would remain stable without any agglomeration or flocculation, due to the electrostatic repulsion between them. Unless otherwise stated, KOH/t-BuOK have the same mass fraction with Kevlar. The optimal concentration range was determined to be 0.01–2.0 wt%. At concentrations below 0.01 wt%, the ANF content was too low for effective gel formation, while exceeding 2.0 wt% increased dispersion viscosity, restricting ANF mobility.

Electro-manipulating of negative-charged aramid nanofibers

The experimental setup employed an aramid colliodal suspension with three distinct concentrations: 0.2 wt%, 0.5 wt%, and 1.0 wt%. A custom fixture was designed to accommodate the electrode configuration, consisting of a 1.0 mm-thick carbon plate anode and a 1.0 mm-thick stainless steel cathode, positioned parallel to each other with a fixed facing-distance of 10 mm. Beyond carbon electrodes, viable anode alternatives encompass stainless steel, titanium, nickel alloys, platinum-group metals and so on. Selection criteria include: (1) insolubility in DMSO, (2) resistance to alkaline corrosion, (3) electrochemical stability against anodic oxidation, while simultaneously ensuring sufficient conductivity. These electrodes were connected to the respective terminals of a direct current (DC) Power Supply (alternating current is not applicable) to establish the required electric field.

Microscopic observation of the EM behavior of ANFs

Thin cathode and anode electrodes were positioned on a microscope slide with a 1 cm interelectrode gap and secured on the microscope stage. The aramid nanofibers (ANF) dispersion was introduced between the electrodes and covered with a coverslip. Upon application of a DC voltage, ANFs migrated toward the anode and formed a gel. The orientation behavior of nanofibers within the gel matrix was analyzed using polarizing microscopy (Supplementary Fig. 5).

Preparation of EM-AC aerogel

The EM-AC colloidal wet gels, formed via electrophoretic assembly and electrochemical gelation, were subjected to solvent exchange with ethanol at room temperature for a minimum of six cycles over two days. Subsequently, the gels were dried using circulating supercritical CO_2 fluid at 40 °C and 10 MPa for at least 10 hours to ensure the complete replacement of ethanol by supercritical CO_2. Depressurization was only initiated after confirming no further ethanol release from the gas vent. As a result, the EM-AC aerogels were successfully obtained.

^{1}H NMR spectra were recorded on a Bruker Ascend 400 MH_Z NMR spectrometer at room temperature with deuterated DMSO as the solvent.

Scanning electron microscopy (SEM)

The morphology of the obtained aerogels was characterized by scanning electron microscopy (SEM, S-4800, Hitachi, Japan) at an acceleration voltage of 5 kV.

Fourier transform infrared spectroscopy

The structure of the samples was determined by the Fourier Transform Infrared Spectroscopy (FTIR 5700, FL, USA) over 64 scans recorded with a resolution wavelength of 4 cm^{-1}.

The pore size distribution and average pore diameter were analyzed by the Barrett-Joyner-Halenda (BJH) nitrogen adsorption and desorption method (ASAP 2020, Micromeritics, USA), and the specific surface area and pore volume were determined by the Brunauer-Emmett-Teller (BET) method, based on the amount of N_2 adsorbed at pressure $0.05 < P/P_0 < 0.3$.

Infrared thermal images were taken by an Infrared camera (Escalab 250 Xi, Thermo Scientific, USA), the working distance was about 30 cm.

The thermal conductivity of the samples was measured by a transient hot-wire method (TC3010L, XIATECH Co., Ltd., China).

The temperature of samples was monitored and recorded with thermal couples connected to a temperature controller (Hangzhou Supmea Co., Ltd., China).

The mechanical properties of the samples were conducted by an Instron 3365 tensile testing machine with a gauge length of 10 mm at a loading rate of 0.5 mm•min^{-1}. More than 3 samples were test for each condition.

X-ray diffraction (XRD) analysis was carried out with a Bruker D8 Advanced spectrometer, using Cu Kα radiation at 40 kV and 40 mA. The scattering angle (2θ) was ranged from 5° to 60°.

The thermal decomposition behavior of aerogel film was studied by differential thermal analysis (TG 209F1 Libra thermogravimetric analyzer).

Raman spectra were recorded on a LabRam HR Raman spectrometer with 50 W He-Ne laser operating at 632 nm with a CCD deter.

The orientation of the aramid colliodal aerogel film is measured by small-angle X-ray scattering (SAXS, Nano STAR, Bruker-AXS).

Area-specific resistance and proton conductivity:

The electrochemical impedance spectroscopy (EIS) of the film was measured using a CHI660E electrochemical workstation (manufactured by Shanghai Chenhua Instrument Co., Ltd.). The specific testing procedure was as follows: the film with a known thickness (L) was assembled between the two compartments of a through-plane conductivity cell, with each compartment filled with an electrolyte solution (3 M H_2SO_4). The active area of the film was denoted as A. After the open-circuit voltage stabilized, the EIS measurement was conducted with a frequency sweep range of 1–10^5 Hz and an AC amplitude of 5 mV. The system resistance with the film was recorded as r_1, while that without the membrane was recorded as r_2. The area-specific resistance (R) and conductivity (σ) of the film were calculated using the following equations:

$R = (r_1\text{-}r_2) \times A$; $\sigma = L / R$

Data availability

The data supporting the findings provided within this Article and its Supplementary Information are available from the corresponding author on request. Source data are provided with this paper.

References

1. Wang, Q. et al. Dioxybenzene-bridged hydrophobic silica aerogels with enhanced textural and mechanical properties. *Microporous Mesoporous Mater.* **294**, 109863 (2020).
2. Pierre, A. C. & Pajonk, G. M. Chemistry of aerogels and their applications. *Chem. Rev.* **102**, 4243–4266 (2002).
3. Yu, Z. et al. Fire-retardant and thermally insulating phenolic-silica aerogels. *Angew. Chem. Int. Ed.* **57**, 4538–4542 (2018).
4. Si, Y. et al. Superelastic and superhydrophobic nanofiber-assembled cellular aerogels for effective separation of oil/water emulsions. *ACS Nano* **9**, 3791–3799 (2015).
5. Zhu, C. et al. Supercapacitors based on three-dimensional hierarchical graphene aerogels with periodic macropores. *Nano Lett.* **16**, 3448–3456 (2016).
6. Du, Y. et al. Reaction-spun transparent silica aerogel fibers. *ACS Nano* **14**, 11919–11928 (2020).
7. Zhao, S. et al. Additive manufacturing of silica aerogels. *Nature* **584**, 387–392 (2020).
8. Ji, X., Du, Y. & Zhang, X. Elaborate size-tuning of silica aerogel building blocks enables laser-driven lighting. *Adv. Mater.* **34**, 2107168 (2022).
9. Ziegler, C. et al. Modern inorganic aerogels. *Angew. Chem. Int. Ed.* **56**, 13200–13221 (2017).
10. Luo, W. et al. Solution processed boron nitride nanosheets: synthesis, assemblies and emerging applications. *Adv. Funct. Mater.* **27**, 1701450 (2017).
11. Chen, Y. et al. Recent progress on nanocellulose aerogels: preparation, modification, composite fabrication, applications. *Adv. Mater.* **33**, 2005569 (2021).
12. Li, K. et al. 3D MXene architectures for efficient energy storage and conversion. *Adv. Funct. Mater.* **30**, 2000842 (2020).
13. Hayward, R. C., Saville, D. A. & Aksay, I. A. Electrophoretic assembly of colloidal crystals with optically tunable micropatterns. *Nature* **404**, 56–59 (2000).
14. Li, X. et al. Multiparticle synergistic electrophoretic deposition strategy for high-efficiency and high-resolution displays. *ACS Nano* **18**, 17715–17724 (2024).
15. Hewa-Rahinduwage, C. C. et al. Reversible electrochemical gelation of metal chalcogenide quantum dots. *J. Am. Chem. Soc.* **142**, 12207–12215 (2020).
16. Yang, M. et al. Dispersions of aramid nanofibers: a new nanoscale building block. *ACS Nano* **5**, 6945–6954 (2011).
17. Yang, B., Wang, L., Zhang, M., Luo, J. & Ding, X. Time saving, high-efficiency approaches to fabricate aramid nanofibers. *ACS Nano* **13**, 7886–7897 (2019).
18. Han, Z. M. et al. Fast and massive production of aramid nanofibers via molecule intercalation. *J. Am. Chem. Soc.* **147**, 7939–7949 (2025).
19. Ding, Y. et al. Visible microfluidic deprotonation for aramid nanofibers as building blocks of cascade-microfluidic-processed colloidal aerogels. *Adv. Mater.* **36**, 2400101 (2024).
20. Zhu, J. et al. Branched aramid nanofibers. *Angew. Chem. Int. Ed.* **56**, 11744–11748 (2017).
21. Li, L. et al. Folk arts-inspired twice-coagulated configuration-editable tough aerogels enabled by transformable gel precursors. *Nat. Commun.* **14**, 8450 (2023).
22. Wu, J. et al. Acid-assisted toughening aramid aerogel monoliths with ultralow thermal conductivity and superior tensile toughness. *Adv. Funct. Mater.* **34**, 2307072 (2024).
23. Hu, Y. et al. Proton donor-regulated mechanically robust aramid nanofiber aerogel membranes for high-temperature thermal insulation. *ACS Nano* **16**, 5984–5993 (2022).
24. Li, L., Lyu, J., Cheng, Q., Fu, C. & Zhang, X. Versatile recyclable Kevlar nanofibrous aerogels enabled by destabilizing dynamic balance strategy. *Adv. Fiber Mater.* **5**, 1050–1062 (2023).
25. Yang, B. et al. Fabrication, applications, and prospects of aramid nanofiber. *Adv. Funct. Mater.* **30**, 2000186 (2020).
26. Tu, R. et al. Alignment controlled aramid nanofiber-assembled films. *Adv. Funct. Mater.* **34**, 2315422 (2024).
27. Ji, H., Feng, S. & Yang, M. Controlled structural relaxation of aramid nanofibers for superstretchable polymer fibers with high toughness and heat resistance. *ACS Nano* **18**, 18548–18559 (2024).

28. Han, Y. et al. Highly thermally conductive aramid nanofiber composite films with synchronous visible/infrared camouflages and information encryption. *Angew. Chem. Int. Ed.* **136**, 202401538 (2024).
29. Lee, M. et al. Network of cyano-p-aramid nanofibres creates ultrastiff and water-rich hydrospongels. *Nat. Mater.* **23**, 414–423 (2024).
30. Liu, H. et al. Robust and multifunctional kirigami electronics with a tough and permeable aramid nanofiber framework. *Adv. Mater.* **34**, 2207350–2207362 (2022).
31. Lyu, J., Li, L. & Zhang, X. Nanoporous aramid colloidal aerogels: design, fabrication, and performance. *Prog. Polym. Sci.* **163**, 101945 (2025).
32. Li, M. et al. Controllable strong and ultralight aramid nanofiber-based aerogel fibers for thermal insulation applications. *Adv. Fiber Mater.* **4**, 1267–1277 (2022).
33. Wu, T. et al. Liquid-infused aerogel membrane with reverse functions enables on-demand emulsification and demulsification. *Nat. Water* **2**, 899–910 (2024).
34. Wen, Z. et al. Aerogel fibers made via generic sol-gel centrifugal spinning strategy enable dynamic removal of volatile organic compounds from high-flux gas. *Adv. Funct. Mater.* **34**, 2407221 (2024).
35. Cheng, Q. et al. General suspended printing strategy toward programmatically spatial Kevlar aerogels. *ACS Nano* **16**, 4905–4916 (2022).
36. Qiu, G. et al. A method for electrodepositing aramid III nanofibers on copper electrodes. *Mater. Lett.* **340**, 134137 (2023).
37. Xu, T. et al. Nanocellulose-assisted construction of multifunctional MXene-based aerogels with engineering biomimetic texture for pressure sensor and compressible electrode. *Nano-Micro Lett.* **15**, 98 (2023).
38. Liu, Z., Lyu, J., Fang, D. & Zhang, X. Nanofibrous Kevlar aerogel threads for thermal insulation in harsh environments. *ACS Nano* **13**, 5703–5711 (2019).
39. Zheng, Y. et al. Directional water collection on wetted spider silk. *Nature* **463**, 640–643 (2010).
40. Sheng, Z. & Zhang, X. Mimicking polar bear hairs in aerogel fibers. *Science* **382**, 1358–1359 (2023).
41. Yan, K. et al. High-throughput clean-up of viscous oil spills enabled by a gel-coated mesh filter. *Nat. Sustain.* **6**, 1654–1662 (2023).
42. Yang, M. & Kotov, N. A. Quantitative biomimetics of high-performance materials. *Nat. Rev. Mater.* **10**, 382–395 (2025).

Acknowledgements

We are grateful for the support from the National Natural Science Foundation of China (52173052 to X.Z. and 52203021 to L.L.), the Natural Science Foundation of Jiangsu Province (BK20220296 to L.L.), the Postdoctoral Fellowship Program of CPSF (GZB20250244 to L.L.) and Suzhou Science and Technology Plan (SYC2022125 to X.Z.).

Author contributions

X.Z. and L.L. conceived the idea and designed the experiments; X.Z. supervised the project; L.L. and R.Y. conducted the experiments. The data were analysed and processed by L.L. and X.Z.; L.L. prepared the manuscript; Z.S. and X.Z. contributed to the revision.

Competing interests

The authors declare no competing interests.

Additional information

Supplementary information The online version contains supplementary material available at https://doi.org/10.1038/s41467-025-63827-y.

Correspondence and requests for materials should be addressed to Xuetong Zhang.

Peer review information *Nature Communications* thanks Hao Bai and the other, anonymous, reviewer(s) for their contribution to the peer review of this work. A peer review file is available.